J Mater Sci (2017) 52:12476–12485

Metals

Selective laser melting of H13: microstructure and residual stress

J. J. Yan[1], D. L. Zheng[1,2], H. X. Li[1], X. Jia[1], J. F. Sun[2], Y. L. Li[3], M. Qian[4], and M. Yan[1,*]

[1] Department of Materials Science and Engineering and Shenzhen Key Laboratory for Additive Manufacturing of High-performance Materials, South University of Science and Technology of China, Shenzhen 518055, China
[2] School of Materials Science and Engineering, Harbin Institute of Technology, Harbin 150001, China
[3] Key Lab for Robot and Welding Automation of Jiangxi Province, Mechanical and Electrical Engineering School, Nanchang University, Nanchang 330031, China
[4] Centre for Additive Manufacture, School of Engineering, RMIT University, Melbourne, VIC 3000, Australia

Received: 7 April 2017
Accepted: 10 July 2017
Published online: 17 July 2017

ABSTRACT

In this research, samples of the H13 steel, a commonly used hot work tool steel in the die/mould manufacturing industry, were additively manufactured using selective laser melting (SLM). Their as-built microstructures were characterised in detail using transmission electron microscopy (TEM) and compared with that of the conventionally manufactured H13 (as-supplied). SLM resulted in the formation of martensite and also its partial decomposition into fine α-Fe and Fe_3C precipitates along with retained austenite. TEM analyses further revealed that the lattice of the resulting α-Fe phase is slightly distorted due to enhanced Cr, Mo and V contents. Substantially high residual stresses in the range of 940–1420 MPa were detected in the as-built H13 samples compared with its yield strength of ~1650 MPa. In addition, it was identified that the high residual stress existed from just about two additive layers (100 μm) above the substrate along the build direction. The high residual stresses were mainly attributed to the martensitic transformation that occurred during SLM. The research findings of this study suggest that the substantially high residual stresses can be easily problematic in the AM of intricate H13 dies or moulds by SLM.

Introduction

H13 is a typical hot work tool steel that is alloyed with elements of Cr, V, Mo, Mn and Si to enable its superior thermal strength, good red hardness and excellent resistance to thermal fatigue and wear. It resists softening up to 540 °C and is widely used to make dies for hot forging, hot extrusion or high-pressure casting of low-melting point metals and alloys such as aluminium and magnesium alloys [1].

Additive manufacturing (AM) builds parts from three-dimensional (3D) digital models typically by a

Address correspondence to E-mail: yanm@sustc.edu.cn

DOI 10.1007/s10853-017-1380-3

layer additive process. The availability of affordable ≥400 W fibre laser since 2007 has significantly stimulated the development and application of metal AM over the last decade [2–4]. Die or mould making is a costly and time-consuming process. AM, however, has the potential to transform the die-making industry. Firstly, the lead time for mould making can be greatly shortened, from months to days as quality moulds can be printed directly from 3D design models [5, 6]. Secondly, the metallurgical bonding that forms between layers of metallic materials during AM can ensure nearly full density and good mechanical properties for mould applications [7–12]. Finally, the advantage to realise conformal cooling is a unique and unrivalled attribute of AM to the mould making industry [13, 14]. Consequently, AM of hot work steels including H13 has attracted increasing attention [15–23].

Selective laser melting (SLM) is a powder-bed-fusion-based AM process. Aside from being able to produce intricate moulds with a nearly full density, SLM is often accompanied by a fast cooling rate, which, on the one hand, can produce a refined microstructure [8, 24, 25]. This, however, can entail large residual stresses or distortion due to steep thermal gradients and/or significant phase transformation stresses [26–28]. For example, Lu et al. [14] found that the residual stress in SLM-fabricated Inconel 718 alloy samples was about 200 MPa, affected by the laser scanning strategy. Griffith et al. [29] used a holographic-hole drilling technique to determine the magnitude and distribution of residual stress in H13 steel samples fabricated by a laser engineered net shaping technology and reported that the residual stress was up to 260 MPa. Li et al. [30] studied the residual stress issue during SLM using a coupled thermo-mechanical model. They found that the residual stress on the top layer of the sample was related to the laser scanning strategy adopted: longitudinal residual stress (~ 350 MPa) was greater than that was measured crosswise in the vertical sequential scanning mode; the residual stress decreased more or less linearly when moving downwards along the built direction. Apart from these studies, high compressive residual stresses (~800 MPa) were measured from spray-formed (a rapid solidification-based AM process) H13 steel samples [31]. The process is similar to SLM in some ways: both processes are solidification-based layer AM processes with a high cooling rate.

From the aforementioned studies, it can tentatively be concluded that the residual stress arising from laser processing is both material and laser scanning strategy dependent, and the stress level can be significant, e.g. close to or even greater than half the yield stress of the material. The potential consequences include (a) decreased geometrical accuracy and stability achievable by the printed material [32]; (b) distortion, cracking or even breakage of parts during SLM or post-processing [14, 33–35]; (c) (if the stress is in tensile) decreased fatigue strength and resistance to stress corrosion [36, 37]. In particular, distortion caused by residual stresses can be a major concern in the AM of intricate dies or moulds by SLM. As such, the steel substrate used in the SLM process often needs to be sufficiently thick and strong in order to counter the potential distortion of the part being built. Also, the as-built parts need to be annealed for stress relief. Owing to the stringent requirement for dimensional accuracy, it is important to understand the magnitude and state of residual stresses in the as-built dies or moulds.

In this study, nearly full dense H13 steel samples were made using the SLM technique. High-angle X-ray radiation (XRD) was then used to characterise the residual stress in the as-built H13 samples. Optical microscopy (OM), scanning electron microscopy (SEM) and TEM were used to understand the microstructural details. We found that the residual stress in some samples exceeded even 1000 MPa. The corresponding stress relief heat treatment therefore may have to have both the microstructure of the as-built H13 and the high residual stress discovered thoroughly considered.

Experimental

SLM of the H13 tool steel

Spherical, gas-atomised H13 steel powder in the size range 25–44 μm was used. Its chemical composition is listed in Table 1. An SLM Solutions 250 HL facility (400 W Yb:YAG laser) was used. Cubic samples ($10 \times 10 \times 10$ mm^3) were produced at a laser power of 150 W, a scan speed of 300 mm/s using an

Table 1 Chemical composition of the H13 powder used in this study

Element	Fe	Cr	Mo	Si	V	Mn	C
wt %	Bal.	5.20	1.23	1.12	1.10	0.41	0.41

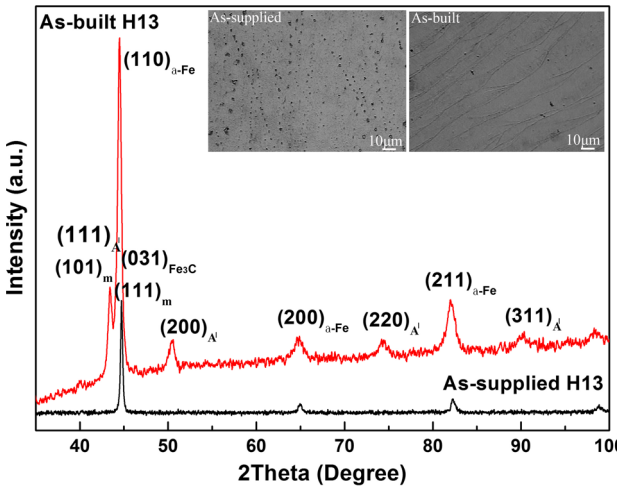

Figure 1 XRD spectra of the as-supplied (i.e. as-purchased) and as-built H13 steel samples. In this figure, A′ stands for the retained austenite phase and m denotes the martensite phase. Figure *insets* are OM micrographs of the as-supplied and as-printed H13 steel samples.

alternate raster pattern and a hatch spacing of 50 μm under argon (Ar). A detailed study of the SLM process of this alloy can also be found in [18]. A 316L stainless steel substrate was used and kept at 200 °C during SLM. For comparative analysis, conventionally produced H13 supplied by the UDDEHOLM ORVAR®SUPREME was analysed, referred to as 'as-supplied H13' hereafter. It was austenitised at 1025 °C for 30 min, followed by air cooling, and then tempered at 610 °C for 2 h.

Characterisation of residual stress, microstructure and microhardness

Residual stress can be assessed using a hole drilling approach, neutron diffraction and X-ray diffraction (XRD). We used the high-angle XRD approach, which is reliable, rapid and non-destructive with a measurement uncertainty of ~5% [38]. The experiments were conducted on an XRD instrument (at 20 kV and 4 mA) purposely designed for the stress measurement. The target material is Cr Kα with a wavelength of 2.291 Å. Peak from the (211) plane of the α-Fe phase was measured by centring at the 2θ value of 156.4°. Slice samples (~0.5 mm thick) were prepared from as-built cubes using a high-precision low-speed diamond saw. They were analysed without polishing to ensure minimised external influences on the as-built microstructure as well as residual stress. Detailed locations of the high-angle XRD sample

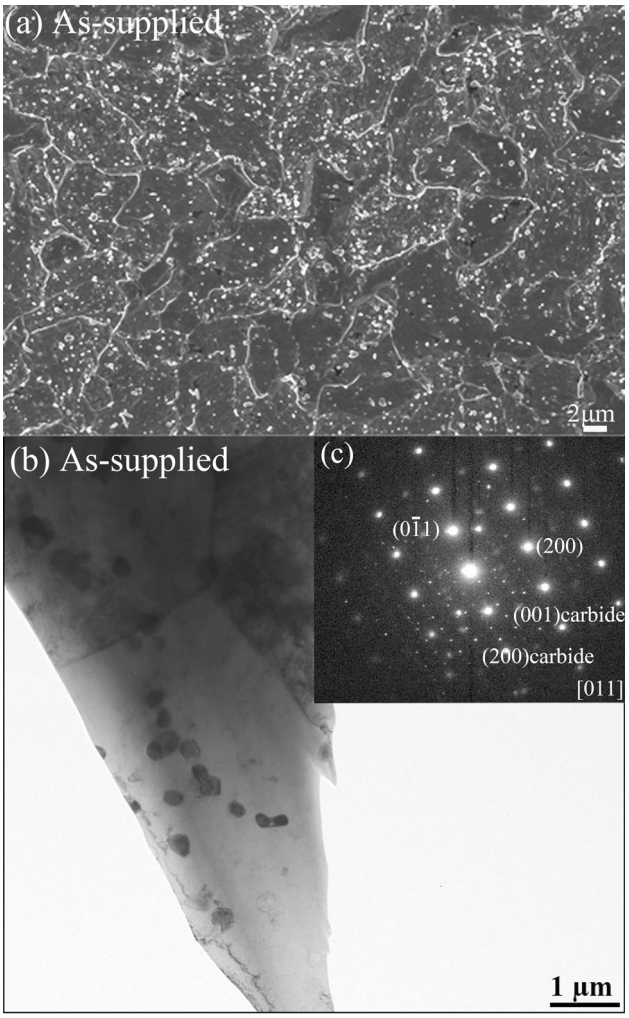

Figure 2 **a** SEM image for the as-supplied H13 showing α-Fe and cementite (Fe_3C), and **b** TEM image reveals that there is an additional carbide phase, i.e. the $(Cr,Fe)_7C_3$ phase, except the Fe_3C phase.

slices are indicated in Fig. 7a. The analysis was focused on the central region of each sample slice using a ϕ2 mm XRD beam aperture.

The phase constitutions of both the as-supplied and as-built H13 samples were investigated using a lab XRD (Rigaku SmartLab) equipped with a high-flux X-ray copper source (9 kW power). The scan rate was 1.5 °min^{-1} in the 2θ angular range of (20–100)°. The microstructure was characterised using scanning electron microscopy (SEM, Merlin, ZEISS, Germany; 10 kV) and TEM (JEM-2010F, 200 kV). TEM samples were prepared by twin jet electropolishing at −30 °C, in a solution of 5% $HClO_4$ + 95% C_2H_5OH (vol.%). A thin layer of gold coating (~ 5 nm thick) was applied

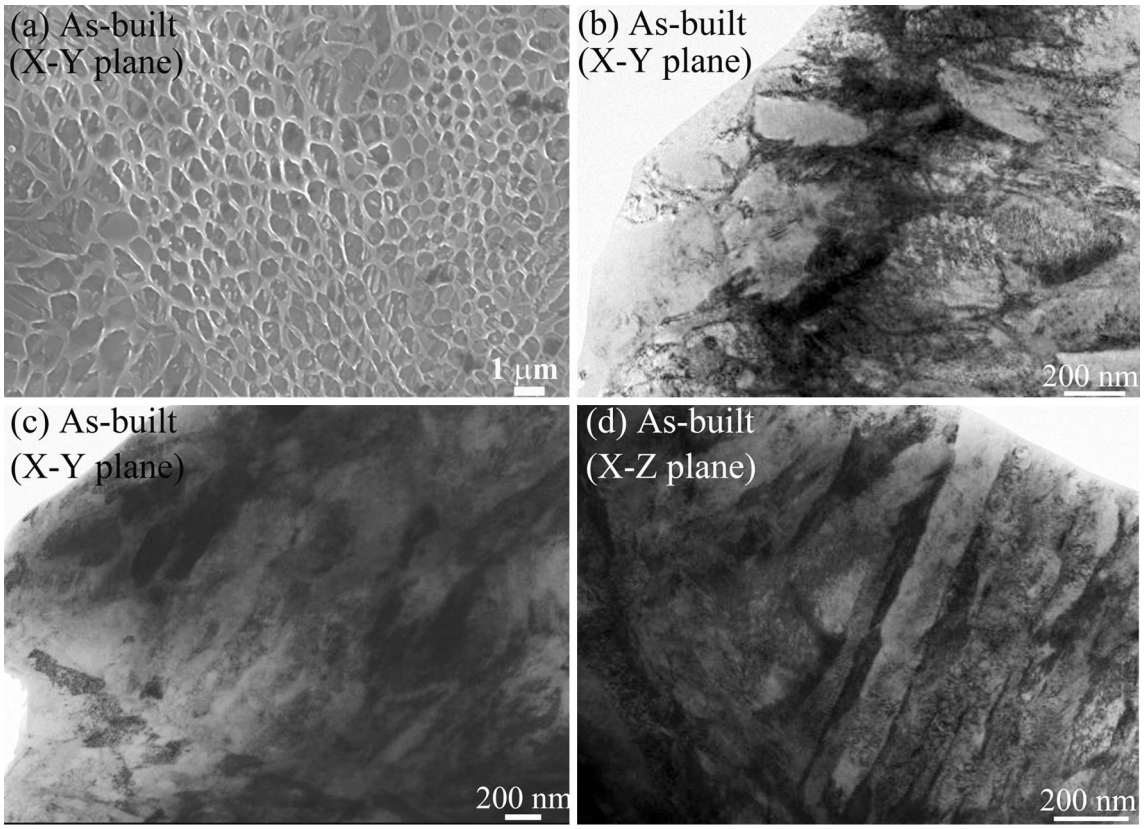

Figure 3 SEM and TEM images for the as-built H13: **a** SEM image for the topmost surface, **b** TEM-BF image for the sample position located at the bottom of the build, **c** TEM-BF image for the sample position located at the middle of the build, and **d** TEM-BF image for the sample that was taken along the build direction and from centre of the build.

on top of each TEM sample using a Q150T sputter coater for calibrating the camera length of the TEM as an internal standard. Digital Micrograph version 3.7.4 was used to analyse the TEM results. Density of the as-built H13 was measured by the Archimedes method. Hardness was measured using an HXD-1000TMC/LCD microhardness tester, with a dwell time of 10 s at a load of 500 gf.

Results

Preliminary characterisation by XRD and optical microscopy

Figure 1 shows the XRD results for both the as-supplied and the as-built H13 with insets showing their optical microstructures. The as-supplied H13 contains dispersed secondary particles, while the microstructure of the as-built SLM H13 is featured by fine strips. An analysis of the XRD data indicates that the as-supplied H13 consists of the *bcc*-structured α-Fe ($a = 2.87$ Å) as the dominating phase, and the cementite Fe_3C phase (orthorhombic structure, with $a = 5.09$ Å, $b = 6.74$ Å and $c = 4.52$ Å), where the strongest peak from the $(031)_{Fe3C}$ overlaps the diffraction from the $(110)_{\alpha\text{-}Fe}$. In contrast, the as-built H13 was found to further contain retained austenite (face-centred-cubic structure, with $a = 3.62$ Å), denoted as the 'A" phase in Fig. 1, and martensite phase ($Fe_{1.86}C_{0.14}$, tetragonal structure with $a = 2.85$ Å and $c = 3.05$ Å), marked out as the 'm' phase in Fig. 1.

The relative density of the as-built H13 reached 99.7 ± 0.1%, which is essentially pore-free and is consistent with microscopic observations. Aside from the microstructure, there is another clear difference in terms of hardness between the as-built H13 and the as-supplied. It was measured to be 57 ± 1 HRC for the as-built H13 versus 45 ± 1 HRC for the as-supplied H13.

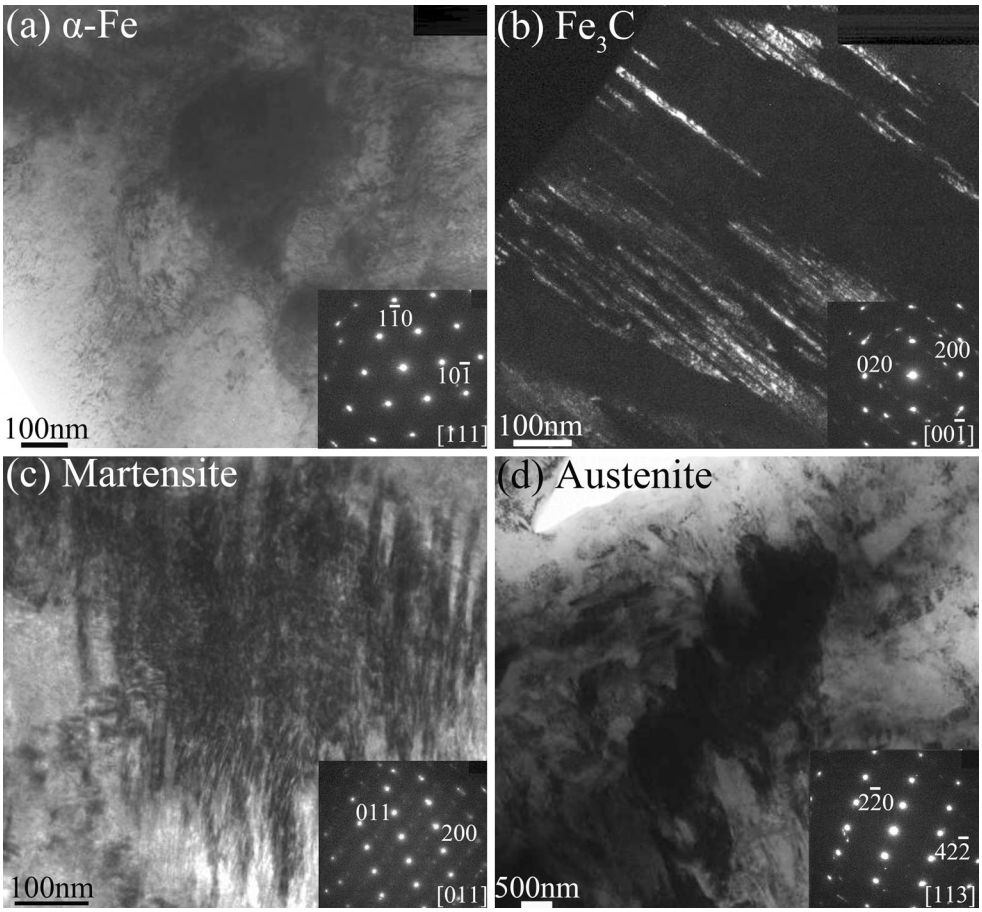

Figure 4 TEM BF and/or DF images and corresponding SAED results for the major phases observed in the as-built H13: **a** the α-Fe phase, **b** the cementite Fe_3C phase (DF image here), **c** the martensite phase and **d** the retained austenite phase.

Detailed characterisation of the as-supplied H13 by SEM and TEM

Figure 2(a) shows an SEM image of the as-supplied H13. Together with the TEM analysis shown in Fig. 2b, c and the XRD spectrum shown in Fig. 1, it can be concluded that matrix of the as-supplied H13 is composed of overwhelmingly α-Fe phase. As pointed out earlier, the secondary phases shown in Fig. 2a are predominantly cementite Fe_3C particles according to the XRD spectrum. TEM characterisation, however, revealed that there is also the $(Cr,Fe)_7C_3$ carbide phase existing in the matrix. The selected area electron diffraction (SAED) patterns of the phases shown in Fig 2b are presented in Fig. 2c. The SAED patterns recorded are complicated. A detailed analysis confirmed that they can be decomposed into diffraction patterns of two phases, i.e. the matrix α-Fe phase, and the $(Cr,Fe)_7C_3$ carbide phase, as shown in Fig. 2c. In addition, it can also be seen from Fig. 2b that both the Fe_3C phase and the $(Cr,Fe)_7C_3$ carbide phase are spherical precipitates of a few hundred nanometers in size.

Detailed characterisation of the as-built H13 by SEM and TEM

Figure 3(a) shows an SEM image of the top layer of the as-built H13. Distinctly different microstructural features from those of the as-supplied H13 were observed. TEM was employed to detail the microstructures in slice samples prepared from the bottom (i.e. close to the substrate, Fig. 3b), and middle (Fig. 3c) of an as-built H13 cube, as well as a sample sliced along the build direction of the cube (Fig. 3d). Theses TEM bright field (BF) images suggest that there is a low level of preferred orientation of grain growth in the x–y plane, while a strong orientation exists along the build direction (z direction).

Further TEM microstructural observations of the as-built H13 are shown in Fig. 4a–d, along with insets to show corresponding SAED results of each phase

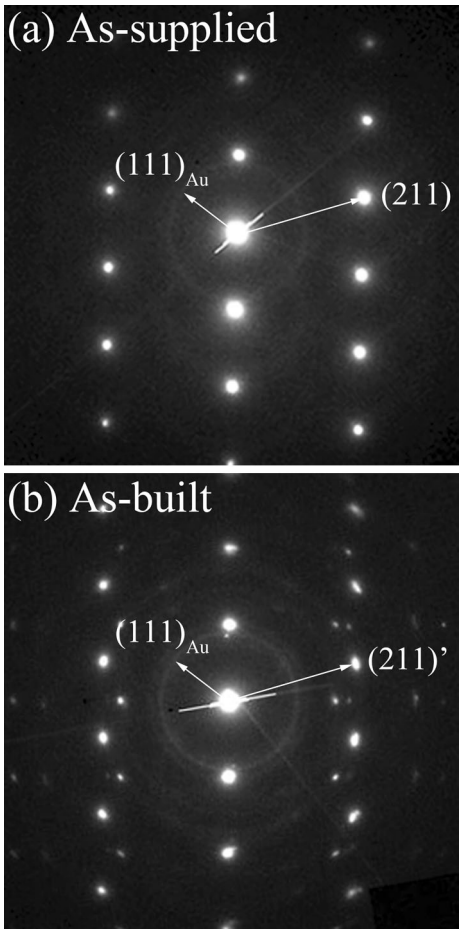

Figure 5 TEM-SAED patterns for the α-Fe phase in the as-supplied H13 **a** and as-built **b** H13 samples. A thin film of Au (~5 nm thick), whose diffraction was used as an internal standard, was coated on each sample.

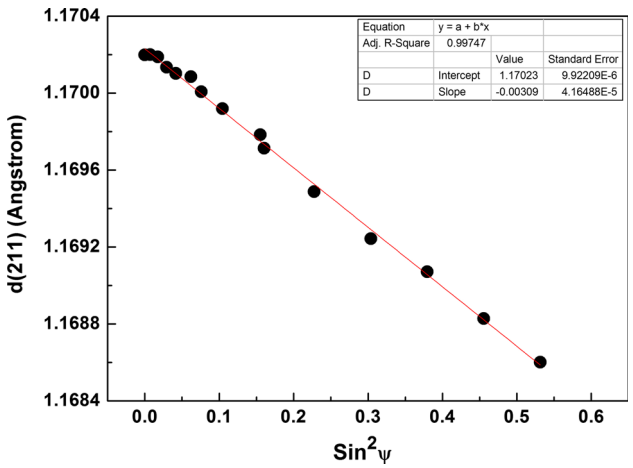

Figure 6 Plot of d versus $\sin^2\psi$ measured for the as-built H13 using high-angle XRD.

included. These SAED results are recognised to be diffracted from the α-Fe phase (Fig. 4a), the Fe_3C phase (Fig. 4b), the martensite phase (Fig. 4c) and the retained austenite phase (γ-Fe, *fcc* with $a = 3.66$ Å; Fig. 4d). The results are consistent with the XRD analyses shown in Fig. 1.

TEM characterisation has also revealed that the lattice of the α-Fe phase in the as-built H13 is slightly distorted. Figure 5 provides the corresponding SAED results to compare the lattice parameters of the matrix phase in the as-supplied (Fig. 5a) and the as-built (Fig. 5b) H13 samples, where a thin layer of Au was used as the internal standard (plane distance of the (111) plane of the Au is known to be 2.35 Å). We found that, in the SAED patterns recorded, the ratio between the $(211)_{\alpha\text{-Fe}}$ diffraction spot and the radius of the Au diffraction ring $(111)_{Au}$ is slightly lower for the as-built H13 than that obtained for the as-supplied, which is 1.958 versus 1.960 (error bar estimated to be ± 0.0005). This indicates that the lattice parameter of the α-Fe phase in the as-built H13 is higher than the as-supplied according to the established relationship of $R{\cdot}d = L{\cdot}\lambda$. We further found that Cr, Mo and V elements are enriched in the α-Fe phase in the as-built H13, see Table 2. This can be attributed to the high cooling rates encountered during SLM. In other words, the α-Fe phase in the as-built H13 is not in an equilibrium state.

Residual stress measurements of the as-built H13

The normal residual stress (σ_x or σ_y where x and y are orthogonal; see Fig. 7) can be calculated from $\sigma = m{\cdot}(E/1 + v)$, where E is Young's modulus, v is Poisson's ratio, and m is the slope of the d versus $\sin^2\psi$ curve [39, 40]. A plot of d versus $\sin^2\psi$ is shown in Fig. 6 based on the experimental data obtained. The slope is -0.00309. H13 has typical value of $E = 210$ GPa and $v = 0.3$ [18, 41]. A high, compressive residual stress of ~ 1000 MPa was obtained from this slice sample. Six similar slice samples were analysed, with their locations in the as-built H13 cube being specified in Fig. 7a. The detailed results are listed in Table 3. Figure 7b summarises the residual stress versus build distance from the substrate, suggesting that residual stress builds up almost immediately after the first two layers during SLM (the stress-free thickness is limited to ~100 μm). It is also noted that the residual stress is distributed almost across the entire as-built material,

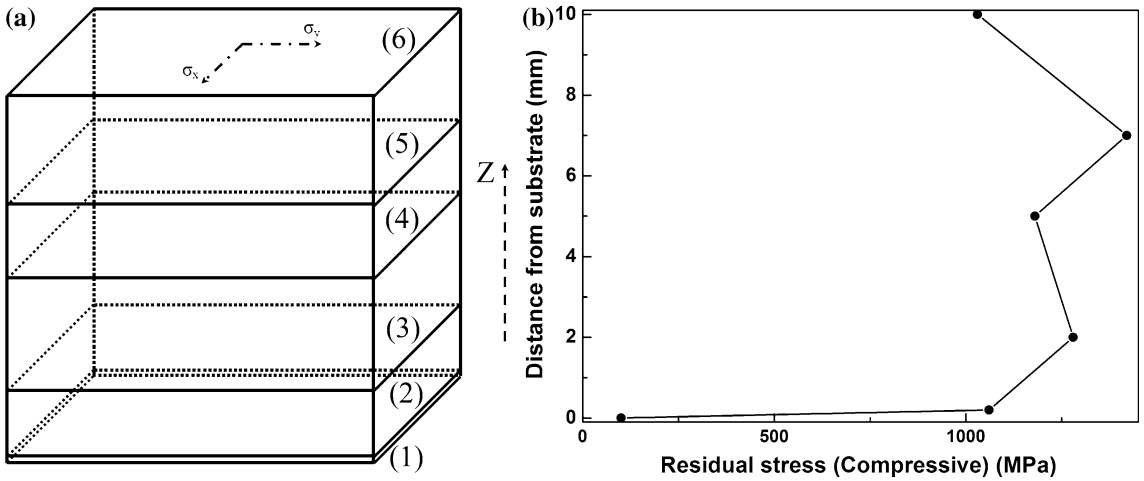

Figure 7 **a** Schematic illustration of the locations of sample slices analysed using high-angle XRD and **b** residual stress distribution along the build direction (*z* axis) of the as-built H13.

Table 2 Chemical composition of the α-Fe phase in the as-built and the as-supplied H13 measured by TEM–EDX (data in at.%; error bar ±0.2 at.%)

	Fe	Cr	Mo	Si	V	Mn	C
As-built	84.6	5.4	0.6	1.8	0.9	0.9	5.8
As-forged	93.0	3.4	0.3	0.4	–	0.1	2.8

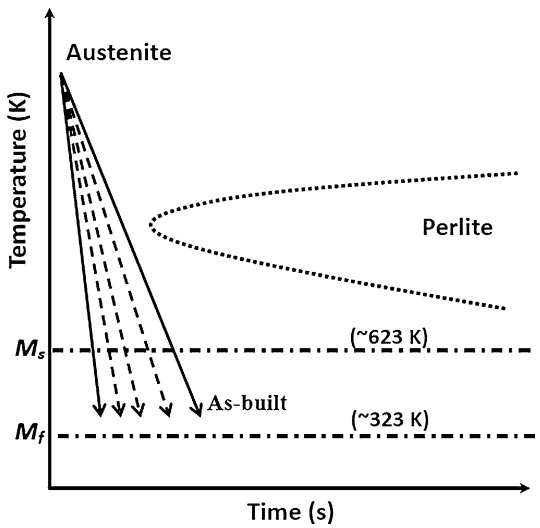

Figure 8 Schematic illustration of the cooling conditions proposed for the as-built H13; the actual cooling rate at different locations can vary over a wide range due to the cyclic thermal conditions that occur during SLM. The M_s and M_f temperatures of the H13 steel are indicated in the figure.

ranging from ~940 to ~1420 MPa, compared to the yield strength of about 1650 MPa for the as-supplied H13 [18, 41] (Fig. 8).

Table 3 Residual stress of the as-built H13 measured using high-angle XRD (error bar ±5%)

Sample	Stress (φ = 0°, MPa)	Stress (φ = 90°, MPa)
1	−1030	−940
2	−1420	−1220
3	−1180	−1230
4	−1280	−1160
5	−1060	−1050
6	−100	6

Discussion

The experimental results and analyses presented above have indicated that: (1) AM by SLM enabled the formation of martensite and also its partial decomposition into α-Fe and Fe_3C in the as-built H13; and (2) the SLM-fabricated H13 has a high-level residual stress in the as-built condition (Table 3).

Research has shown that the cooling rate during laser powder deposition of the H13 steel can reach ~1.83×10^4 K/s (which is similarly (1.2–4.0) × 10^4 K/s for laser powder deposition of Ti-6Al-4 V) [42]. The critical cooling rate for martensitic transformation in the H13 steel is ~20 K/s, while its M_s temperature is about 613 K (=350 °C) and its M_f temperature is about 323 K (=50 °C) [18, 41]. The observation of the martensite phase in the as-built H13 is therefore understandable. In fact, the significantly higher hardness of the as-built H13 (= 57 ± 1 HRC) versus that of the as-supplied H13 (=45 ± 1 HRC) also supports the martensitic structure observed in the in the as-built H13 (a marginal

increase in hardness can be attributed to the refined microstructure). Owing to different cooling rates in different regions of the cube and the cyclic thermal effects from successively build layers, some of the martensite structures may have decomposed into α-Fe and carbides (i.e. Fe_3C).

With regard to the residual stress, the total strain ($\Delta\varepsilon$) developed during the cooling stage can be expressed as a combination of thermal (T), elastic (e), plastic (p) and phase transformation (Tr) factors: $\Delta\varepsilon = \Delta\varepsilon^T + \Delta\varepsilon^e + \Delta\varepsilon^p + \Delta\varepsilon^{Tr}$ [43]. The H13 steel has yield strength ($\sigma_{0.2}$) of ~1650 MPa [18, 41]. The high-level residual stress detected in the as-built H13 is thus still in the elastic deformation range. If we assume that the elastic strain is fully recovered (i.e. zero) in the as-built H13 and no plastic deformation has occurred, then the overall residual stress level can be regarded as a balanced result between the strain ($\Delta\varepsilon^{Tr}$) which is induced by phase transformation and the strain ($\Delta\varepsilon^T$) which is induced by the thermal gradient. The former normally leads to compressive residual stress via the relationship $\Delta\sigma = E{\cdot}\Delta\varepsilon^{Tr}$, but the latter normally corresponds to tensile stress. Murakawa et al. [44] and Francis et al. [45] have shown that if the martensitic phase transformation temperature (e.g. M_s) is lower than 400 °C, the overall residual stress can be a large, compressive one. Since the M_s temperature of the H13 steel is merely 350 °C, it can be concluded that the martensitic phase transformation is the key reason for the high-level compressive residual stress detected, which is in good agreement with Refs. [44, 45].

Normally the high residual stress detected in the as-built metallic materials should be relieved. Stress relieving of the as-supplied H13 is typically carried out in the range of 600–650 °C for 2 h. SLM-fabricated H13 may need a different annealing treatment to accommodate both its microstructural features and the high residual stress detected. These require another detailed, specific study to make a good investigation.

Conclusions

Detailed microstructural characterisation and residual stress measurements have been conducted for the SLM-fabricated H13 in the as-built condition, using the as-supplied H13 as a reference. The following conclusions can be drawn from this research.

1. High-angle XRD has been used to measure the residual stress in the as-built H13, which shows rather high compressive residual stresses that vary in the range of 940–1420 MPa. The residual stress exists almost throughout the as-built H13. The martensitic transformation that occurs during the SLM of the H13 steel is proposed to be the main contributing factor to the high compressive residual stress detected.
2. Detailed microstructural analysis has shown that the major crystalline phases in the as-built H13 are α-Fe, Fe_3C, retained austenite (γ-Fe) and martensitic phase. In comparison, α-Fe, Fe_3C and $(Cr,Fe)_7C_3$ are the three detectable phases in the as-supplied H13. The α-Fe phase in the as-built H13 has a slightly higher lattice parameter than that in the as-supplied H13 due to higher contents of Cr, Mo and V.

Acknowledgements

The authors thank Dr. Matthew Rowles of the University of Melbourne for his measurement of the residual stress and Prof. M. Brandt and Mr Maciej Mazur of RMIT University for providing the as-built H13 samples. The study is financially supported by the Vice Chancellor Research Fund of the South University of Science and Technology of China (SUSTC), and Shenzhen Science and Technology Innovation Commission under project No. ZDSYS201703031748354.

Compliance with ethical standards

Conflict of interest The authors declare that they have no conflict of interest.

References

[1] ASM International Handbook Committee (1990) Properties and selection: irons, steels, and high performance alloys. In: Metals handbook, vol 1, 10th edn.

[2] Morgan RH, Papworth AJ, Sutcliffe C, Fox P, O'Nell W (2002) High density net shape components by direct laser re-melting of single-phase powders. J Mater Sci 37:3093–3100. doi:10.1023/A:1016185606642

[3] Everhart Wes, Sawyer Eric, Neidt Tod, Dinardo Joe, Brown Ben (2016) The effect of surface finish on tensile behavior of

additively manufactured tensile bars. J Mater Sci 51:3836–3845. doi:10.1007/s10853-015-9702-9

[4] Sander J, Hufenbach J, Bleckmann M, Giebeler L, Wendrock H, Oswald S, Gemming T, Eckert J, Kuhn U (2017) Selective laser melting of ultra-high-strength TRIP steel: processing, microstructure, and properties. J Mater Sci 52:4944–4956. doi:10.1007/s10853-016-0731-9

[5] Altan T, Lilly BW, Kruth JP, König W, Tönshoff HK, van Luttervelt CA, Khairy AB (1993) Advanced techniques for die and mold manufacturing. CIRP Ann Manuf Technol 42:707–716

[6] Altan T, Lilly B, Yen YC, Altan T (2001) Manufacturing of dies and molds. CIRP Ann Manuf Technol 50:404–422

[7] Yan YN, Li SJ, Zhang RJ, Lin F, Wu RD, Lu QP, Xiong Z, Wang XH (2009) Rapid prototyping and manufacturing technology: Principle, representative technics, applications, and development trends. Tsinghua Sci Technol 14:1–12

[8] Sander J, Hufenbach J, Giebeler L, Wendrock H, Kühn U, Eckert J (2016) Microstructure and properties of FeCrMoVC tool steel produced by selective laser melting. Mater Des 89:335–341

[9] Xue L (2010) Laser consolidation: a rapid manufacturing process for making net-shape functional components. In: Lawrence JR, Pou J, Low DKY, Toyserkani E (Eds) Advances in laser materials processing, 1st edn. pp 492–534

[10] Yap CY, Chua CK, Dong ZL (2016) An effective analytical model of selective laser melting. Virtual Phys Prototyp 11:21–26

[11] Chen JY, Xue LJ, Wang SH (2011) Experimental studies on process-induced morphological characteristics of macro- and microstructures in laser consolidated alloys. J Mater Sci 46:5859–5875. doi:10.1007/s10853-011-5543-3

[12] Yan M, Xu W, Gargusch MS, Tang HP, Brandt M, Qian M (2014) A review of the effect of oxygen on room-temperature ductility of titanium and titanium alloys. Powder Metall 57:251–257

[13] Brooks H, Brigden K (2016) Design of conformal cooling layers with self-supporting lattices for additively manufactured tooling. Addit Manuf 11:16–22

[14] Lu YJ, Wu SQ, Gan YL, Huang TT, Yang CG, Lin JJ, Lin JX (2015) Study on the microstructure, mechanical property and residual stress of SLM Inconel-718 alloy manufactured by differing island scanning strategy. Opt Laser Technol 75:197–206

[15] Mazumder J, Choi J, Nagarathnam K, Koch J, Hetzner D (1997) The direct metal deposition of H13 tool steel for 3-D components. J Miner Met Mater Soc 49:55–60

[16] Ahn DG (2011) Applications of laser assisted metal rapid tooling process to manufacture of molding and forming tools—state of the art. Int J Precis Eng Manuf 12:925–938

[17] Maziasz PJ, Payzant EA, Schlienger ME, McHugh KM (1998) Residual stresses and microstructure of H13 steel formed by combining two different direct fabrication methods. Scr Mater 39:1471–1476

[18] Mazur Maciej, Leary Martin, McMillan Matthew, Elambasseril Joe, Brandt Milan (2016) SLM additive manufacture of H13 tool steel with conformal cooling and structural lattices. Rapid Prototyp J 22(3):504–518

[19] Sander J, Hufenbach J, Giebeler L, Wendrock H, Kühn U, Eckert J (2016) Microstructure and properties of FeCrMoVC tool steel produced by selective laser melting. Mater Des 89:335–341

[20] Safka J, Ackermann M, Volesk L (2016) Structural properties of H13 tool steel parts produced with use of selective laser melting technology. In: Journal of physics: conference series, vol 709. Article id: 012004

[21] AlMangour Bandar, Grzesiak Dariusz, Yang Jenn-Ming (2017) Selective laser melting of TiB2/H13 steel nanocomposites: influence of hot isostatic pressing post-treatment. J Mater Process Technol 244:344–353

[22] AlMangour Bandar, Grzesiak Dariusz, Yang Jenn-Ming (2016) Nanocrystalline TiC-reinforced H13 steel matrix nanocomposites fabricated by selective laser melting. Mater Des 96:150–161

[23] AlMangour Bandar, Frankline Yu, Yang Jenn-Ming, Grzesiak Dariusz (2017) Selective laser melting of TiC/H13 steel bulk-form nanocomposites with variations in processing parameters. MRS Commun 7:1–6

[24] Bremen S, Meiners W, Diatlov A (2012) Selective laser melting. Laser Tech J 9:33–38

[25] Kumar S (2014) Selective laser sintering/melting. Compr Mater Process Mater Sci Mater Eng 10:93–134

[26] Li YL, Gu DD (2014) Parametric analysis of thermal behavior during selective laser melting additive manufacturing of aluminum alloy powder. Mater Des 63:856–867

[27] Mercelis P, Kruth JP (2006) Residual stresses in selective laser sintering and selective laser melting. Rapid Prototyp J 12:254–265

[28] Gu DD, He BB (2016) Finite element simulation and experimental investigation of residual stresses in selective laser melted Ti–Ni shape memory alloy. Comput Mater Sci 117:221–232

[29] Griffith ML, Schlienger ME, Harwell LD, Oliver MS, Baldwin MD, Ensz MT, Essien M, Brooks J, Robino CV, Smugeresky JE, Hofmeister WH, Wert MJ, Nelson DV (1999) Understanding thermal behavior in the LENS process. Mater Des 20:107–113

[30] Li C, Fu CH, Guo YB, Fang FZ (2016) A multiscale modeling approach for fast prediction of part distortion in

selective laser melting. J Mater Process Technol 229:703–712

[31] Lin YJ, McHugh KM, Zhou YZ, Lavernia EJ (2006) Microstructure and hardness of spray-formed chromium-containing steel tooling. Scr Mater 55:581–584

[32] Zaeh MF, Branner G (2009) Investigations on residual stresses and deformations in selective laser melting. Prod Eng 4:35–45

[33] Yadroitsev I, Yadroitsava I (2015) Evaluation of residual stress in stainless steel 316L and Ti6Al4V samples produced by selective laser melting. Virtual Phys Prototyp 10:67–76

[34] Jiang WH, Kovacevic R (2007) Laser deposited TiC/H13 tool steel composite coatings and their erosion resistance. J Mater Process Technol 186:331–338

[35] Qiu C, Ravi GA, Dance C, Ranson A, Dilworth S, Attallah MM (2015) Fabrication of large Ti-6Al-4V structures by direct laser deposition. J Alloys Compd 629:351–361

[36] Leuders S, Thöne M, Riemer A, Niendorf T, Tröster T, Richard HA, Maier HJ (2013) On the mechanical behaviour of titanium alloy TiAl6V4 manufactured by selective laser melting: Fatigue resistance and crack growth performance. Int J Fatigue 48:300–307

[37] Lee C, Park H, Yoo J, Lee C, Woo W, Park S (2015) Residual stress and crack initiation in laser clad composite layer with Co-based alloy and WC + NiCr. Appl Surf Sci 345:286–294

[38] Prevey PS (1986) X-ray diffraction residual stress techniques. In: ASM handbook, vol 10, 9th edn. pp 380–392

[39] Kang M, Park G, Jung JG, Kim BH, Lee YK (2015) The effects of annealing temperature and cooling rate on carbide precipitation behavior in H13 hot-work tool steel. J Alloys Compd 627:359–366

[40] Cottam R, Wang J, Luzin V (2014) Characterization of microstructure and residual stress in a 3D H13 tool steel component produced by additive manufacturing. J Mater Res 29:1978–1986

[41] AISI Type H13 Hot Work Tool Steel. http://www.matweb.com/search/datasheet_print.aspx?matguid=e30d1d1038164808a85cf7ba6aa87ef7

[42] Qian M, Xu W, Brant M, Tang HP (2016) Additive manufacturing and post-processing of Ti–6Al–4V for superior mechanical properties. MRS Bull 41:775–783

[43] Hao SX, Liu ZC (2005) A study on continuous cooling transformation (CCT) curves of hot work die steel H13. Spec Steel 26:23–24

[44] Murakawa H, Béreš M, Davies CM, Rashed S, Vega A, Tsunori M, Nikbin KM, Dye D (2010) Effect of low transformation temperature weld filler metal on welding residual stress. Sci Technol Weld Join 15:393–399

[45] Francis JA, Stone HJ, Kundu S, Bhadeshia HKDH, Rogge RB, Withers PJ, Karlsson L (2009) The effects of filler metal transformation temperature on residual stresses in a high strength steel weld. J Press Vessel Technol 131:041401